Chapter 8

Creep Behavior of Age-hardened AXM520 Alloy and NCs

The present chapter aims to explore the microstructural alteration and creep characteristic of the squeeze-cast age-hardened Mg-5.0Al-2.0Ca-0.3Mn (AXM520HT) alloy, as well as AXM520HT+1.0SiC (NC1.0SiCHT) and AXM520HT+2.0SiC (NC2.0SiCHT) (wt.%) nanocomposites (NCs). A correlation of the creep responses of age-hardened AXM520 alloy and its nanocomposites with their initial and creep-deformed microstructures has been established. For the first time, deformation mechanism maps for Mg-Al-Ca alloys and their nanocomposites are constructed. A summary of the microstructures and creep responses of AXM520HT, NC1.0SiCHT and NC2.0SiCHT, is presented at the end of this chapter.

8.1 Hardness response of aged AXM520 alloy and NCs

The AXM520HT alloy, as well as NC1.0SiCHT and NC2.0SiCHT nanocomposites, were subjected to aging at 523 K, and their age-hardening responses were examined by evaluating the microhardness values, as shown in Figure 8.1(a). As anticipated, the values of Vickers hardness of the AXM520HT alloy and its nanocomposites gradually increase with the aging time. The highest hardness responses of the alloy and nanocomposites were achieved following 2 hr of aging at 523 K. The microhardness values then decreased with a further increase in the aging time, confirming over aging of the specimens. At the peak aged condition, the AXM520HT alloy exhibited a hardness of 71.7±1.6 HV, and the values for the NC1.0SiCHT and NC2.0SiCHT were 75.8±2.4 HV and 79.9±1.3 HV, respectively. The hardness values of the alloy and NCs in as-cast conditions were 50.9±2.3, 53.4±1.2, and 56.8±2.2, respectively. Thus, the hardness values of the AXM520HT, NC1.0SiCHT, and NC2.0SiCHT are improved by 40.9, 41.9, and 40.7 %, respectively following aging. The significant improvement in hardness values confirms the beneficial effects of aging.

8.2 Microstructural characterization of aged AXM520 and NCs

The XRD patterns displayed in Figure 8.1(b) correspond to the aged AXM520HT alloy, and nanocomposite samples confirmed the presence of the primary α-Mg phase, i.e., the solid solution of Al, Ca, and Mn in Mg. The solubilities of Al and Ca in Mg at room temperature are limited, and therefore, different intermetallic phases inevitably formed in the AXM520HT alloy. The recorded XRD profile exhibited the characteristics peaks of the $(Mg,Al)_2Ca$ (C36), Al_2Ca (C15), and Al_8Mn_5 intermetallic phases, as shown in the enlarged view of the XRD patterns in Figure 8.1(c). A small peak associated with the SiC phase was observed in NC2.0SiCHT, which confirms the presence of the SiC nanoparticles in the NCs. The SEM micrograph of the AXM520HT alloy at peak-aged conditions in Figure 8.2(a) exhibits the primary α-Mg phase in a dark gray appearance. The C36 phase formed a lamellar morphology with α-Mg phase, i.e., a binary eutectic at the grain boundaries and triple junctions. Another white spherical phase was observed at the α-Mg grain interior. The magnified view of 'a' in Figure 8.2(b) depicts that the C36 phase is discontinuous. Liu et al., in their investigation, showed that the secondary phase became more discontinuous and fragmented in the AXM alloys with increased heat treatment time [142]. A similar morphological change in the secondary phase of the AXM alloys with solutionizing time was reported by Inoue et al. [143]. Figure 8.2(c) presents a magnified micrograph of the AXM520HT alloy, and the corresponding elemental mapping shown in Figure 8.2(d) confirms that the grain boundary phase was enriched with Al and Ca. In addition, the Al and Mn-rich spherical white particles were observed. The EDS analysis results shown in Figure 8.2(e), i.e., Mg-5.0Al-2.4Ca (at.%) taken from the dark gray region, confirm the matrix phase is constituted of α-Mg. The composition of the phase at the grain boundary shown in Figure 8.2(f) was Mg-30.7Al-14.6Ca (at.%), ensuring the formation of the C36 phase. Suzuki et al. [54] reported the morphological alteration of the C36 phase in the AXM-based alloys aged at 573 K for 3600 s. The EDS data obtained from the white spherical particles shown in Figure 8.2(g), i.e., Mg-46.3Al-43.3Mn (at.%), confirms the phase is Al_8Mn_5. Li et al. [56] and Han et al. [52] also confirmed the existence of the Al_8Mn_5 phase, with similar composition in the AXM4204 and AX52 alloys. The micrographs of the aged NC2.0SiCHT in Figure 8.2(h and i) exhibit the fragmented topology of the C36 phase present in it. The discontinuous lamellas of the C36 phase were attributed to a complex solidification process of the melt involved in the presence of solid SiC nanoparticles. In the presence of nanoparticles, the migration of solute atoms from the solid to liquid phase is strongly hindered [96,144]. Therefore, the heterogeneous nucleation site

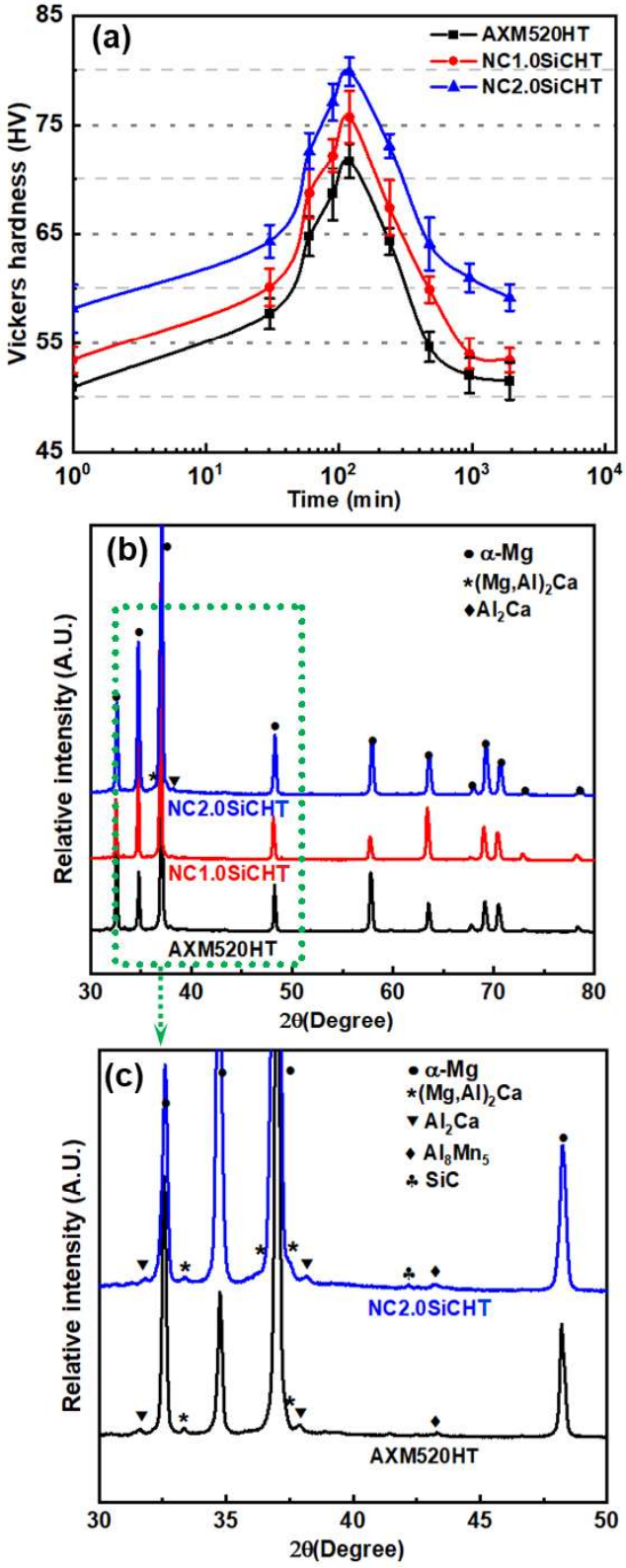

Figure 8.1 (a) Variation of hardness values with aging time for AXM520HT and NCs; (b) XRD pattern acquired from the peak-aged AXM520HT and NCs; (c) magnified view of the 2θ range from 30 to 50 ° for the XRD patterns shown in 'b' for AXM520HT and NC2.0SiCHT.

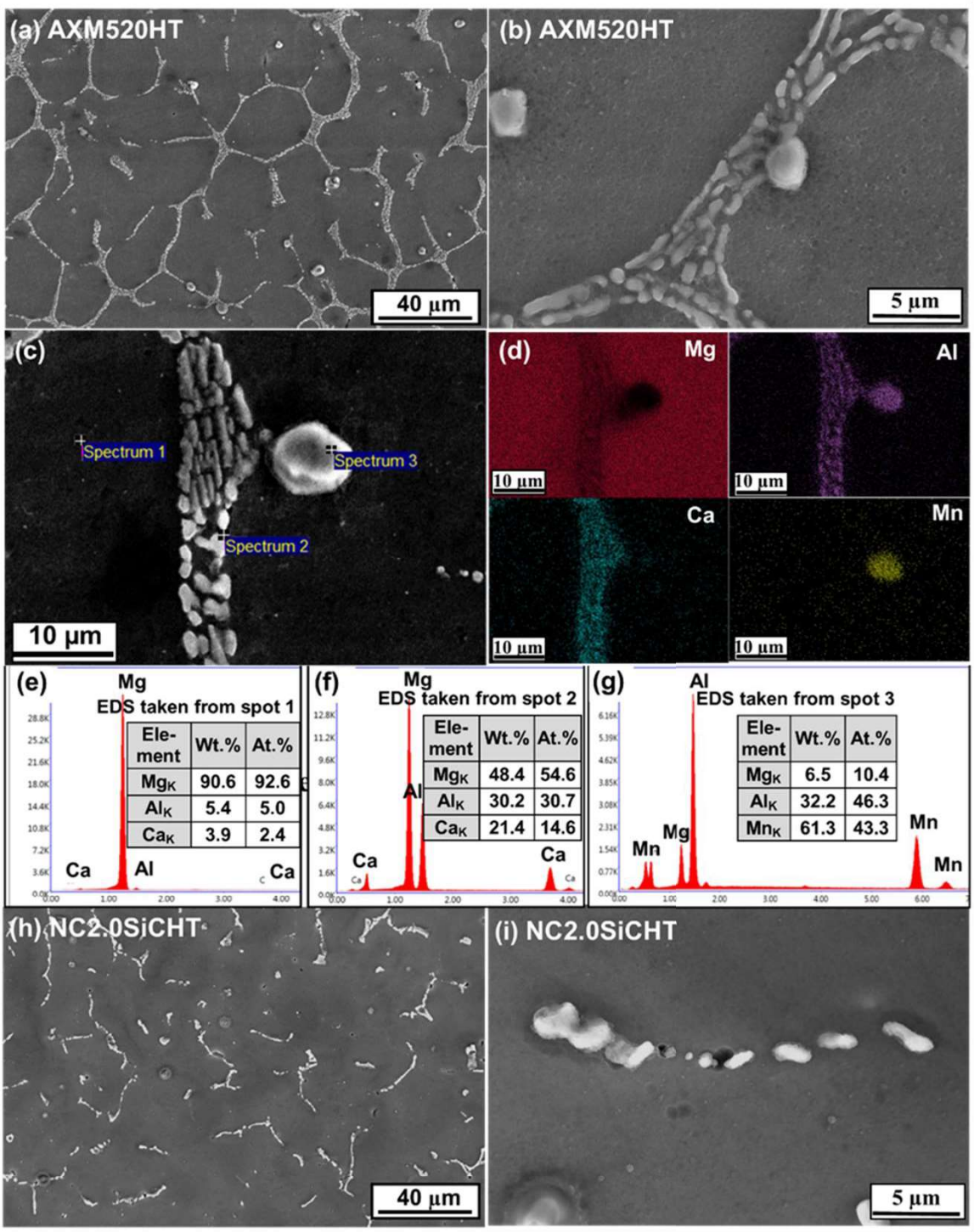

Figure 8.2 (a) SEM micrograph of the aged AXM520HT; enlarged view of 'a' showing the (b) morphologies of C36 and Al_8Mn_5 phases, and (c) regions of elemental mapping and EDS analyses; (d) elemental maps corresponding to 'c'; EDS results from (e) spectrum 1 corresponding to α-Mg, (f) spectrum 2 corresponding to C36, and (g) spectrum 3 corresponding to Al_8Mn_5; (h) SEM micrograph of the aged NC2.0SiCHT; (i) enlarged view of 'h' showing the morphology of C36 phase.

increased and modified the secondary phase's morphology during the casting of the nanocomposites. The TEM micrograph acquired from the α-Mg phase of aged AXM520HT alloy is shown in Figure 8.3(a). Two different precipitates with rod and planner-like morphologies were present in the α-Mg grain interior of the alloy, and the same is seen in the magnified micrograph provided in Figure 8.3(b). Figure 8.3(c) presents the SAED pattern obtained from the same region, displaying a dot pattern characteristic of the α-Mg phase acquired from the [0001] beam direction. Additionally, multiple ring patterns were also observed, and these are from the precipitates formed in the α-Mg grain interior. The 'd' spacing calculated from the smaller ring value was equal to 2.13 Å, confirming the {306} plane of the Al_8Mn_5 phase. The 'd' spacing of the bigger ring is 1.52 Å, confirming the {511} plane of the Al_2Ca (C15) phase. The rod-like precipitates have a length of 85.4±1.6 nm and a width of 10.7±1.3 nm, whereas the planner-type precipitate has a length of 65.3±2.1 nm. The probable precipitates that might form in the AXM alloys are Mg-Al, Mg-Ca, Mg-Mn, Al-Ca, Al-Mn, and Ca-Mn, and their enthalpies of mixing are -2, -6, 35, -20, -70, and 59, respectively. Therefore, the Al-Mn and Al-Ca precipitates formed due to their lower values of enthalpy of mixing [145]. Zuo et al. [62] reported that the rod-like precipitates were enriched with Al and Mn and identified as the Al_8Mn_5 phase. The planar precipitates were identified as the Al_2Ca phase. Nakata et al. [146] reported the formation of planner Al_2Ca precipitates after age-hardening of the AXM10304 alloy. Bian et al. [147] too mentioned the formation of planner Al_2Ca precipitates during age-hardening of AXM alloys and concluded that these semi-coherent precipitates were monolayered G.P. zones. Figure 8.3(d) exhibits the grain interior of NC2.0SiCHT. In the nanocomposites, the rod and planner-like precipitates were also observed. A phase with spherical morphology was also observed, as displayed in Figure 8.3(e). As mentioned earlier, the SAED pattern in Figure 8.3(f) acquired from the region of Figure 8.3(e) exhibits multiple ring patterns that correspond to the Al_8Mn_5 and Al_2Ca phases. Additionally, a ring pattern from the {111} plane of the SiC phase with the d spacing of 2.52 Å was also observed.

8.3 Creep behavior

8.3.1 Creep response and creep mechanism

Figure 8.4(a) compares the time dependency of the impression depth of the age-hardened alloy and nanocomposites at a stress of 435 MPa and temperature of 498 K. All the curves consist

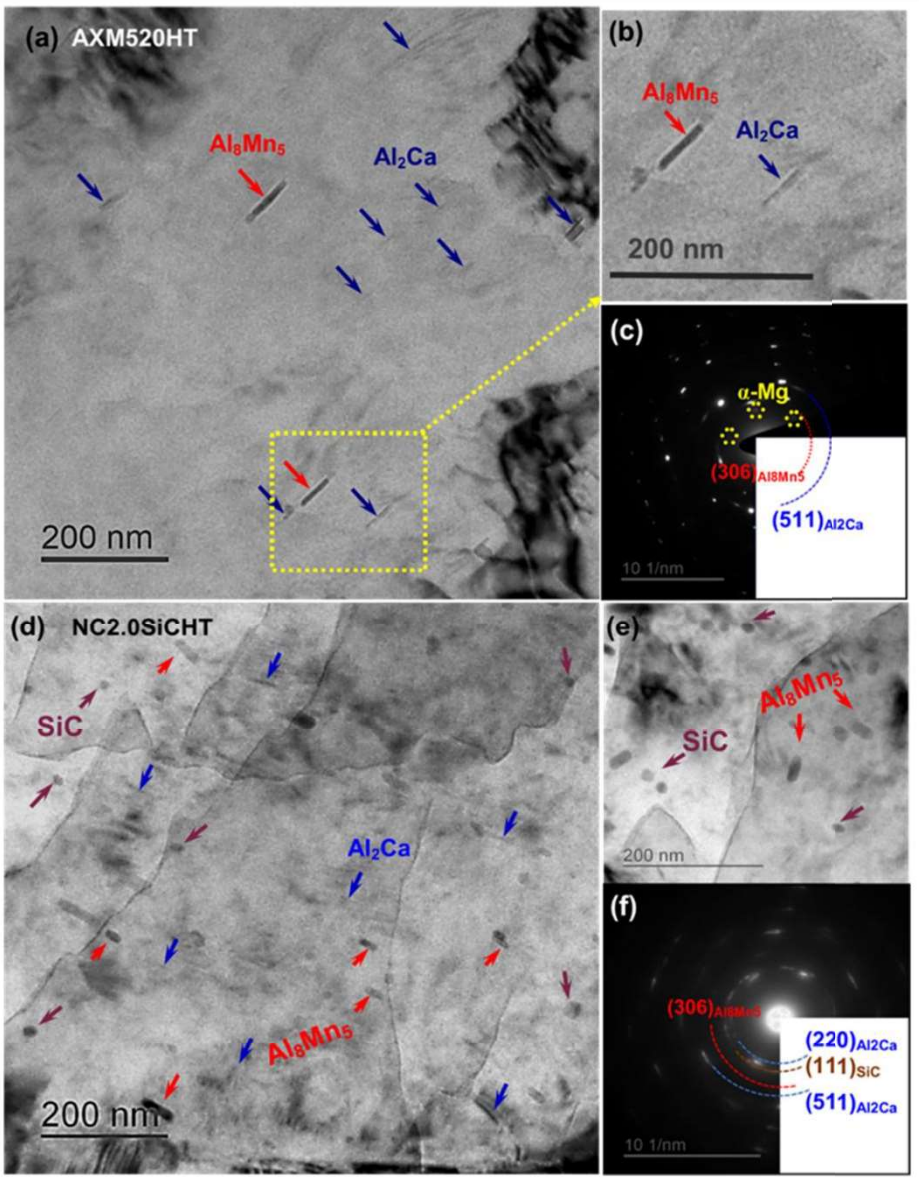

Figure 8.3 (a) TEM image (BF) revealing the precipitates formed in the α-Mg grain interior of AXM520HT; (b) enlarged view of 'a' showing two precipitates with rod and planner-like morphologies, (c) SAED pattern captured from 'a'; (d) TEM image (BF) exhibiting the presence of precipitates and SiC_{np} in the α-Mg grain interior of NC2.0SiCHT; (e) enlarged view of 'd' showing the morphologies of precipitates and dispersed SiC_{np} phase, (f) SAED pattern captured from 'c'

of only two stages of creep deformation (i.e., primary and secondary stages) after instantaneous deformation. The creep curve is divided into three distinct regions in conventional creep testing. However, impression creep curves do not exhibit the tertiary stage due to the test's compressive nature. The indentation depth over a fixed period was lower in the NCs than the alloy, implying that the SiC-dispersed nanocomposites were more creep-resistant than the AXM520HT alloy. The time dependency of the impression velocity of all the samples corresponding to Figure 8.4(a) is depicted in Figure 8.4(b). The impression velocity profile displayed a biphasic trend, wherein the primary stage was marked by a velocity reduction, followed by a stabilization stage in the secondary stage. The balance between strain hardening and recovery rate was the reason for constant steady-state impression velocity in the secondary stage. Figure 8.4(b) also depicts the steady-state impression velocity values with bar diagrams. The nanocomposites exhibited lower steady-state impression velocities than the AXM520HT alloy. The steady-state impression velocities of NC1.0SiCHT and NC2.0SiCHT decreased by 54% and 76%, respectively, compared to the AXM520HT. The measured creep rate in heat treated samples were improved closed to 30 % in all the compositions.

The creep mechanism that controlled the deformation of the alloy and NCs is evaluated by determining the stress exponent (n) and activation energy (Q) values. The well-established Mukherjee-Bird-Dorn equation related to the steady state creep rate ($\dot{\varepsilon}$) for conventional creep tests is given in Eq. 6.1 and reproduced as follows [65].

$$\dot{\varepsilon} = A\frac{Gb}{KT}\left(\frac{b}{d}\right)^{p}\left(\frac{\sigma}{G}\right)^{n} D_o e^{-\frac{Q}{RT}}$$

In this equation, A, G, b, d, D_0, and T are defined as a material constant, shear modulus, burgers vector, grain size, diffusion coefficient, and test temperature, respectively. In an impression creep test $\dot{\varepsilon} = \frac{V_{imp}}{Indentor\ diameter}$ (s^{-1}), and $\sigma = \frac{\sigma_{imp}}{3}(MPa)$, as mentioned in Eq. 6.2.

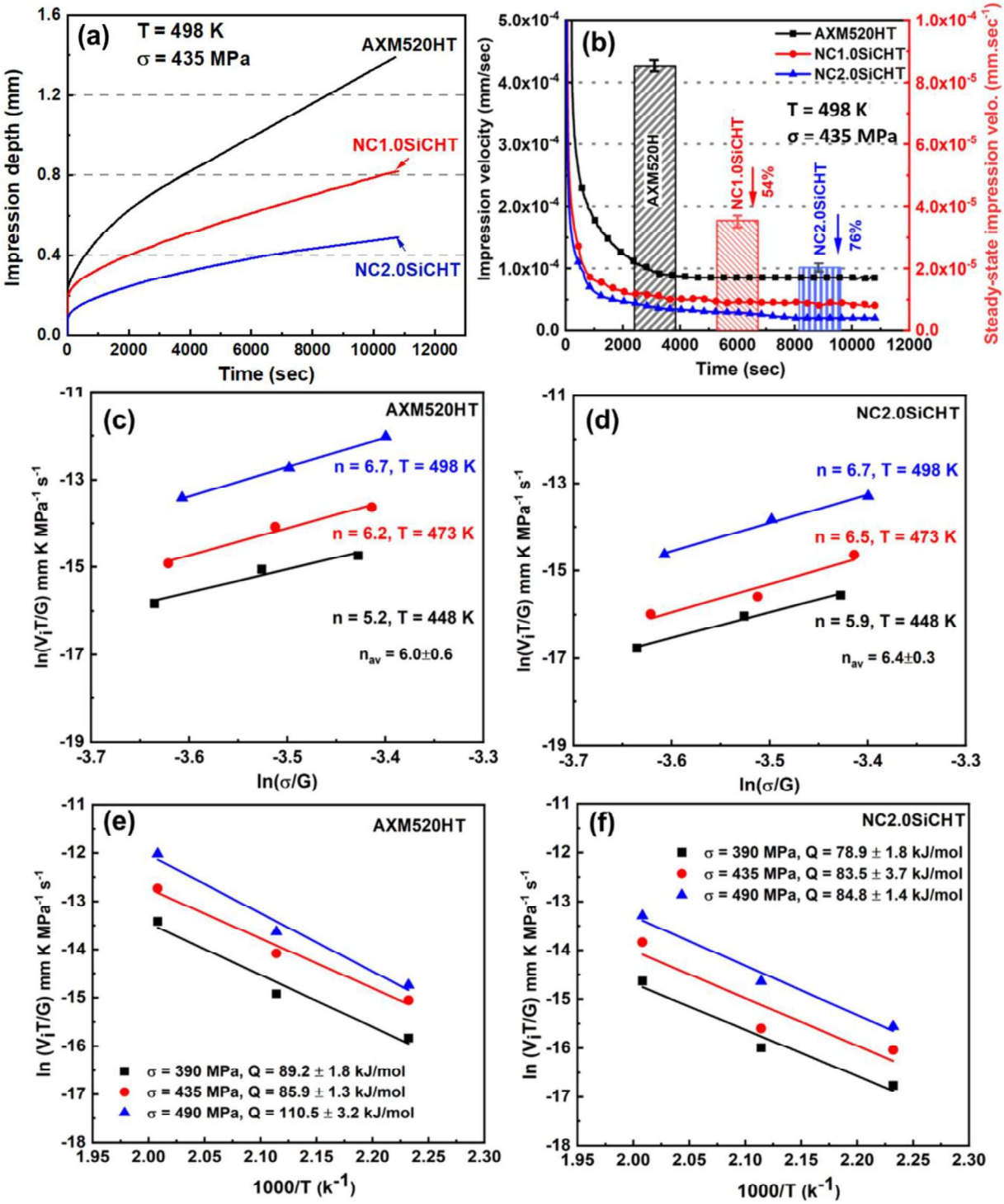

Figure 8.4 (a) Impression depth vs. time plots obtained at 435 MPa and 498 K for the aged AXM520HT and NCs; (b) steady-state impression velocity vs. time plot for AXM520HT and NCs corresponding to 'a'; representative plots showing (c and d) stress and (e and f) temperature dependence of steady-state impression velocities for AXM520HT and NC2.0SiCHT.

Thus, Eq. 6.1 for impression creep is modified as follows, as discussed earlier in Eq. 6.3 [30].

$$\frac{V_{imp}T}{G} = B\left(\frac{\sigma_{imp}}{G}\right)^n e^{\left(-\frac{Q}{RT}\right)}$$

For the heat-treated alloy and NCs, the values of n can be calculated from the slopes of $\ln\left(\frac{V_{imp}T}{G}\right)$ vs. $\ln\left(\frac{\sigma_{imp}}{G}\right)$ plots at a fixed temperature, and the values of Q can be evaluated by multiplying universal gas constant (R = 8.314 $JK^{-1}.mol^{-1}$) with the slope of $\ln\left(\frac{V_{imp}T}{G}\right)$ vs. 1000/T curves at a constant stress. Figure 8.4(c and d) displays the calculations of n values of the AXM520HT and NC2.0SiCHT, respectively, at all tested temperatures. The average n values of the AXM520HT and NC2.0SiCHT were 6.0 ± 0.6 and 6.4 ± 0.3, respectively. The creep deformation mechanism of the alloy and NCs was identified as a dislocation climb based on the calculated stress exponent (n) value. The Q values for the AXM520HT alloy, and NC2.0SiCHT were evaluated as displayed in Figure 8.4(e and f). The Q values for the AXM520HT and NC2.0SiCHT were in the range of 78.9 ± 1.8 to 110.5 ± 3.2 kJ/mol for NC2.0SiCHT. The Q values obtained in the current study are very close to the value responsible for the pipe diffusion of Mg, i.e., 92 kJ/mol. A summary of the n and Q values at different temperatures and stresses for all the samples is given in Table 8.1 and 8.2.

Table 8.1 Summary of the n values obtained from the creep tests at different temperature levels.

Temp. (K)	n		
	AXM520HT	NC1.0SiCHT	NC2.0SiCHT
448	5.2	5.8	5.9
473	6.2	6.4	6.5
498	6.7	6.8	6.7
n_{av}	6.0±0.6	6.3±0.4	6.4±0.3

Table 8.2 Summary of the Q values obtained from the creep tests at different stress levels.

Stress (MPa)	Q (kJ.mol^{-1})		
	AXM520HT	NC1.0SiCHT	NC2.0SiCHT
390	89.2±1.8	86.5±2.9	78.9±1.8
435	85.9±1.3	76.4±0.5	83.5±3.7
480	110.5±3.2	90.2±1.4	84.8±1.4
Q_{av}	95.2±10.9	84.4±5.8	82.4±2.5

8.3.2 Construction of creep mechanism map

The construction of a creep mechanism map is one of the essential aspects of creep study, which can be used in the future as a reference for the selection of stress and temperature range from the application point of view. In the present study, the Mg-Al-Ca (Ca/Al ~0.4) alloy's creep mechanism map was constructed. The construction of the map was achieved by following the equations given in Table 8.3. The material constant value (K_8) during dislocation climb assisted by lattice diffusion can be calculated from the intercept by fitting a straight line through the experimental data plotted in $ln\left(\frac{\dot{\varepsilon}b^2}{D_L}\right)$ vs. $ln\left(\frac{\sigma}{G}\right)$. Similarly, the K_9 value for dislocation climb assisted by pipe diffusion can be estimated from $ln\left(\frac{\dot{\varepsilon}b^2}{D_p}\right)$ vs. $ln\left(\frac{\sigma}{G}\right)$ plot. Figure 8.5(a) displayed the plot for both conditions. The lattice diffusion-controlled data of AX52 [148] alloy showed that the fitted straight line had a slope of 5, equal to the n value during lattice diffusion. The estimated K_8 value was 6.34×10^8. Additionally, the pipe-diffusion-controlled creep of AXM520 and AXM620 was plotted, and the n value was found to be ~7, indicating dislocation climb assisted by pipe diffusion [149]. The K_9 value for the AX alloys was found to be 1.25×10^8. Figure 8.5(b) shows the plot for grain boundary sliding (GBS) condition to estimate the value of K_4 and K_5. The K_4 and K_5 values were estimated using the linear fit method from the $ln\left(\frac{\dot{\varepsilon}d^3}{D_{gb}.b}\right)$ vs. $ln\left(\frac{\sigma}{G}\right)$ and $ln\left(\frac{\dot{\varepsilon}d^2}{D_p}\right)$ vs. $ln\left(\frac{\sigma}{G}\right)$ plots, respectively [18,150,151]. The slope of the linear fit was ~2 for GBS assisted by grain boundary diffusion and ~4 for pipe diffusion assisted GBS. The K_4 and K_5 were estimated as 1.25×10^5 and 1.58×10^5, respectively. Thereafter, the rest of the constant values were taken from the work by Somekawa et al. to construct the entire deformation mechanism map [117]. Figure 8.5(c) exhibits the creep deformation mechanism map in terms of $ln(d)$ vs. $ln\left(\frac{\sigma}{G}\right)$ for the AX alloys at 473 K. The

experimental values from previous literature and current investigations were plotted on the map [18,149-151]. Further, Figure 8.5(d) exhibits a creep deformation mechanism map as a function of $ln\left(\frac{\sigma}{G}\right)$ and (T/T_m) (homologous temperature). The map was constructed by considering grain size (d) as 33 μm, equal to the grain size of NC2.0SiCHT. The creep deformation maps constructed in the present investigation map correctly predict the creep deformation mechanism involved for the Mg-Al-Cal-based alloys and their NCs over a combination of stress, temperature, and grain size range. The maps exhibit that diffusion-based creep can occur only at high temperatures when the grain size is < 100 μm (10^{-4} m) and applied stress is low ($\sigma/G < 10^{-5}$). Therefore, for the targeted application regime (i.e., 473 to 498 K) for the AX-based alloys, the chances of diffusion-based creep are nil. In the present investigation, the creep tests were performed with the applied normalized stress (σ/G) > 10^{-5}, and homologous temperature ranges from 0.4 to 0.6. Based on this, the maps predict that the creep deformation is dominated by dislocation climb in the AXM520 alloy and its NCs, which is already concluded based on the values of n and Q. The grain boundary sliding added by diffusion will dominate when the grain size is below 10 μm [18,150]. However, the boundary between the pipe and lattice-based diffusion is not distinct, which is attributed to the lack of data availability in this regime. Therefore, these newly constructed maps could be used as a reference to predict the creep deformation mechanism for a particular stress, temperature, and grain size range for the AX alloys.

8.4 Microstructural analyses of creep-tested specimens

8.4.1 Observation of deformed region

The indentations produced on the creep-tested (435 MPa and 498 K) specimens of the AXM520HT and NC2.0SiCHT were bisected along the diameter, and the microstructural observations were carried out by taking the regions from the edges of the indenter. The SEM micrographs from the regions are provided in Figure 8.6(a and b). As expected, the three distinct regions are observed under the indenter, which is the characteristic of an indentation. The Hertzian stress distribution below the indentation is understood using Eq. 6.4, as discussed earlier [119].

$$\sigma_z = -\frac{1}{2}\frac{P_m}{(1-\frac{r^2}{a^2})^{1/2}}$$

The indentation test applies a mean pressure of P_m, generating a normal stress of σ_z beneath the indenter.σ_zThe radius of the flat indenter is 'a', and radial distance r is considered from the

Table 8.3 List of equations with constant values employed to construct the creep deformation mechanism maps of the Mg-Al-Ca-based alloys and their nanocomposites.

Creep mechanisms		Equations	Value of material constant (K) (s^{-1})
Diffusional flow	Nabarrow-Herring	$\dot{\varepsilon} = K_1\left(\frac{D_L}{d^2}\right)\left(\frac{Eb^3}{KT}\right)\left(\frac{\sigma}{G}\right)$	14 [117]
	Coble	$\dot{\varepsilon} = K_2\left(\frac{D_{gb}.b}{d^3}\right)\left(\frac{Eb^3}{KT}\right)\left(\frac{\sigma}{G}\right)$	50 [117]
Grain boundary (GB) sliding	Lattice diffusion	$\dot{\varepsilon} = K_3\left(\frac{D_L}{d^2}\right)\left(\frac{\sigma}{G}\right)^2$	1.8×10^{6} [117]
	GB diffusion	$\dot{\varepsilon} = K_4\left(\frac{D_{gb}.b}{d^3}\right)\left(\frac{\sigma}{G}\right)^2$	1.25×10^{5} *
	Pipe diffusion	$\dot{\varepsilon} = K_5\left(\frac{D_p}{d^2}\right)\left(\frac{\sigma}{G}\right)^4$	1.58×10^{5} *
Dislocation climb	Harper-Dorn	$\dot{\varepsilon} = K_6\left(\frac{D_L}{b^2}\right)\left(\frac{Eb^3}{KT}\right)\left(\frac{\sigma}{G}\right)$	7.0×10^{-11} [117]
	Solute drag	$\dot{\varepsilon} = K_7\left(\frac{D_s}{b^2}\right)\left(\frac{\sigma}{G}\right)^3$	3.0×10^{-2} [117]
	Lattice diffusion	$\dot{\varepsilon} = K_8\left(\frac{D_L}{b^2}\right)\left(\frac{\sigma}{G}\right)^5$	6.34×10^{8} *
	Pipe diffusion	$\dot{\varepsilon} = K_9\left(\frac{D_p}{b^2}\right)\left(\frac{\sigma}{G}\right)^7$	1.25×10^{8} *
Equations for diffusional coefficient and G value			
D_p	Pipe diffusion	$3.6\times10^{-5}e^{-92000/kT}$	
D_{gb}	GB Diffusion	$7.7\times10^{-3}e^{-92000/kT}$	
D_L	Lattice diffusion	$1.0\times10^{-4}e^{-135000/kT}$	
D_s	Solute-drag Diffusion	$1.2\times10^{-3}e^{-143000/kT}$	
G (MPa)	Shear modulus	18460 - 8.2×T (MPa)	
b	Burgers vector	3.21×10^{-10} (m)	

*Calculated in the present investigation for the Mg-Al-Ca-based alloys and their nanocomposites from Figure 8.5(a and b)

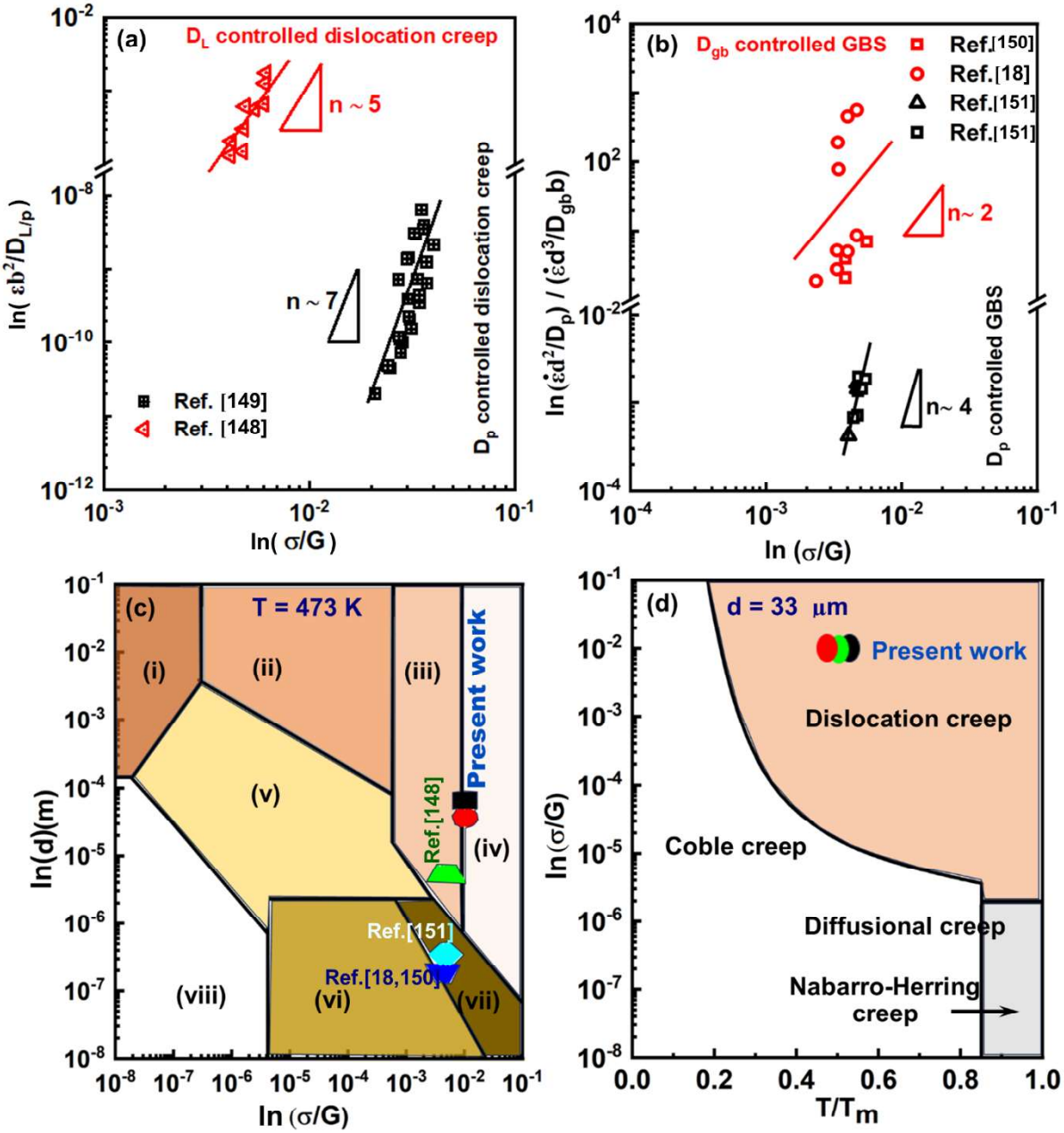

(i) Harper–Dorn creep (n = 1), (ii) Solute drag creep (n = 3), (iii) Climb-controlled creep (n=5) lattice diffusion , (iv) Climb-controlled creep (n = 7) pipe diffusion, (v) GBS lattice diffusion (n = 2), (vi) GBS grain boundary diffusion (n = 2), (vii) GBS pipe diffusion (n = 4), (viii) Diffusional flow (n = 2) coble creep. [117]

Figure 8.5 Diffusion coefficient normalized steady-state strain rate vs. shear modulus normalized applied stress plot exhibiting various deformation mechanisms in Mg-Al-Ca (AX) alloys (a) D_L- and D_p -controlled dislocation creep; (b) D_{gb}- and D_p -controlled grain boundary sliding creep; (c) grain size vs. shear-modulus normalized applied stress plot exhibiting dislocation mechanism map of Mg-Al-Ca (AX) alloys and their nanocomposites at 473 K, and (d) shear modulus normalized applied stress vs. homologous temperature plot for NC2.0SiCHT with grain size of 33 μm.

center of the flat indenter. Below the indenter, at the center point (i.e. r = 0,) σ_z = - 0.5 P_m. Thus, the R1 region, just underneath the indenter, undergoes a minimal deformation and forms a hemispherical hydrostatic stress zone (i.e., dead zone). As the value of 'r' reaches a (i.e., at the indenters' edge), the σ_z value increases drastically and reaches infinity at the indenters' edge. Therefore, the region marked as R2 experiences localized shear force and undergoes shear deformation. The spread of region R2 exhibits the deformation resistance offered by the material during the creep test at a particular stress and temperature. The region R2 is wider in AXM520HT than NC2.0SiC, implying the inferior creep response of the former. The region away from the indention, i.e., region R3, shows an undeformed zone similar to that of the untested region. This region experienced negligible stress, and accordingly, the microstructural alteration was negligible. The magnified view of R2 of AXM520HT shows that the secondary phase was utterly broken, whereas the same remains intact within the α-Mg matrix in the case of NC2.0SiCHT. This implies that the presence of SiC_{np} in NC2.0SiCHT gave additional strengthening in the NC2.0SiCHT matrix compared to the AXM520HT.

The EBSD data were acquired from the highly deformed regions, i.e., the regions at the edges of the indenter, as shown in Figure 8.6(a and b) of the creep tested (498 K and 435 MPa) AXM520HT and NC2.0SiCHT. The grain boundary map corresponding to the region is shown in Figure 8.7(a and b). The grain boundary misorientation value lower than 15 º is defined as the low-angle grain boundaries (LAGBs), and the misorientation above 15 º is considered as the high-angle grain boundaries (HAGBs). The results show that in both the alloy and NCs, the highly deformed regions are populated with HAGBs. In addition, the twin boundaries inside grain interiors of all the samples were observed. The formation of twins during deformation of Mg alloy and composites is well known owing to their limited slip systems [152]. Figure 8.7(c and d) exhibits the misorientation map corresponding to Figure 8.7(a and b). The results show the frequency of HAGBs was high in all the cases. In addition, the contribution of different twins in HAGBs is also shown. The formation of double twin (38º, $\{10\bar{1}1\}$-$\{10\bar{1}2\}$), compression twin (56º, $\{10\bar{1}1\}$), and extension twin (86º, $\{10\bar{1}2\}$) is observed in the alloy and NCs [152-154]. The formation of $\{10\bar{1}1\}$ and $\{10\bar{1}2\}$ twins took place by rotating the twinned lattice around the $<1\bar{2}10>$ direction by 56º and 86º, respectively. Similarly, the double twin was formed by rotating the c-axis around $<1\bar{2}10>$ direction for both the primary and secondary twins. Their existence in creep-tested AXM520HT and NC2.0SiCHT can be further confirmed by the inverse pole figure maps shown in Figure 8.7(e). In all the cases, the inverse pole figure

maps confirm the presence of <1$\bar{2}$10> oriented boundaries. The inverse pole figure maps in the range of 84-88º indicate that many HGBs are oriented along <1$\bar{2}$10>. This result indicates that the deformed samples are populated with extension twins. The comparison of the twin-frequency percentage of the AXM520HT and NC2.0SiCHT is displayed in Figure 8.7(f). In all the twin modes, it has been observed that the percentage of twins in the creep-tested specimen of NC2.0SiCHT was lower than that of the AXM520HT alloy. This indicates the presence of nanoparticles successfully hindered the growth of the twins in NCs, contributing to the lower deformation of the NCs compared to the AXM520HT. Therefore, in the creep tests, the SiC_{np} dispersed AXM520HT composites showed a better creep response than the AXM520HT. Shi et al. [155] concluded that nano-sized precipitates hindered the twin growth in Mg alloys. Antony et al. [156] also confirmed that the particles present in the grain boundaries of Mg alloys also hindered twin growth. Leu et al. [157] concluded that the precipitates provided back stress, which significantly restricted the development of twins in the AZ91 alloy.

8.4.2 Characterization of twinning and dislocations

The twined formed during creep deformation (T = 498 K and σ = 435 MPa) of the NC2.0SiCHT specimen is shown in Figure 8.8(a to d). Figure 8.8(a) exhibits a lamellar-type twin in the deformed sample of NC2.0SiCHT. The twin was bound by two twin boundaries (TB) separated from the matrix of the NC. Numerous dislocations, nano-precipitates of Al_8Mn_5 and Al_2Ca phases, and dispersed SiC_{np} phase were observed near the TB. The presence of nano-precipitates and SiC_{np} at TB suggests that they hindered the twin growth in the α-Mg matrix. Several other researchers also reported that the precipitates and dispersed phases hindered twin growth in Mg alloys [158,159]. This also supports the claim that the lower creep deformation of NC2.0SiCHT was owing to twin growth restriction provided by the dispersed SiC_{np} phase.

Figure 8.8(b) exhibits the SAED pattern captured from TB region displayed in Figure 8.8(a). SAED pattern analysis reveals that the twinned lattice rotated around 86 º along <1$\bar{2}$10> to produce {10$\bar{1}$2} twin. The twin system was classified as an extension twin of {10$\bar{1}$2}<10$\bar{1}$1>. Therefore, the twinning plane was identified as {10$\bar{1}$2} and the <10$\bar{1}$1> was the direction of the twin. The brightfield (BF) image in Figure 8.8(c) exhibits another twin variant produced during the creep deformation. The corresponding SAED pattern is provided in Figure 8.8(d). SAED pattern analysis reveals that the matrix and twin lattice were oriented by 37.4 º. Further, indexing confirms that the twin was {10$\bar{1}$1}-{10$\bar{1}$2} double twin. The double twin formed due

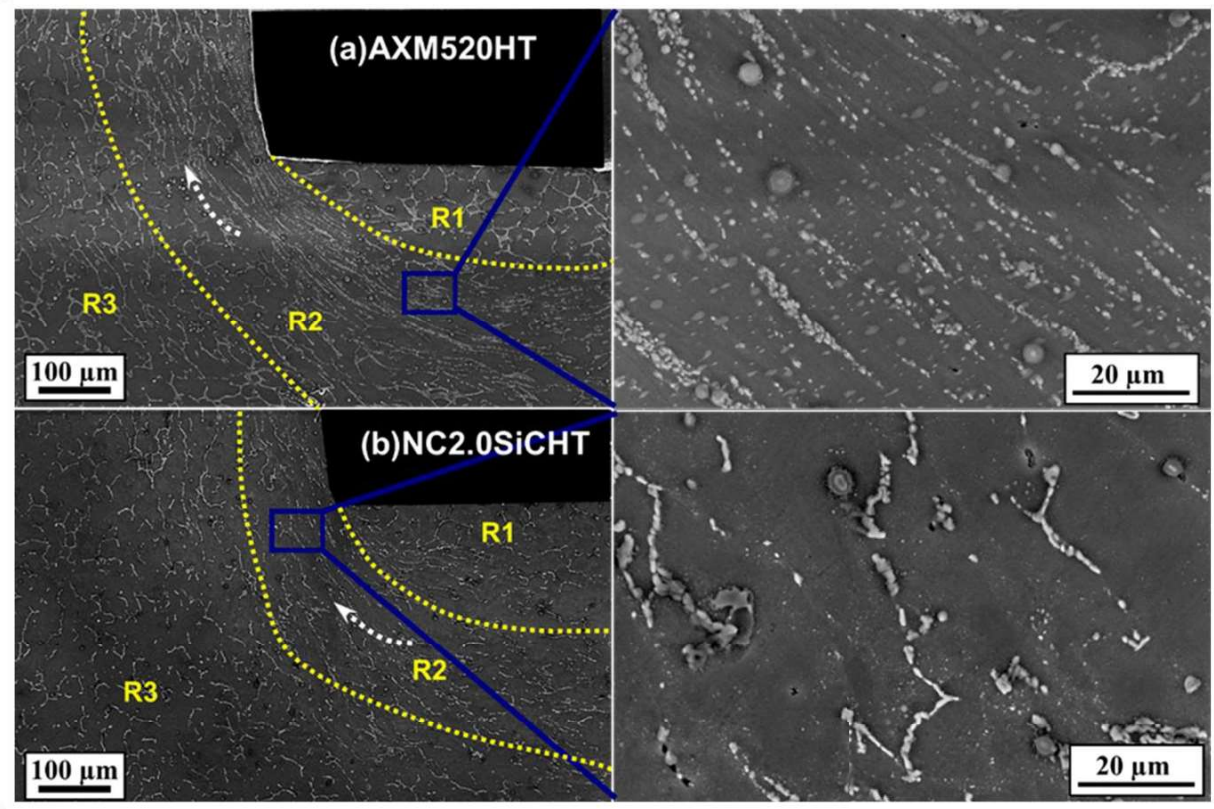

Figure 8.6 SEM micrographs exhibiting the deformation flow pattern in different regions under impressions on the creep-tested (T = 498 K, σ = 435 MPa) specimens of (a) AXM520HT, as well as (b) NC2.0SiCHT.

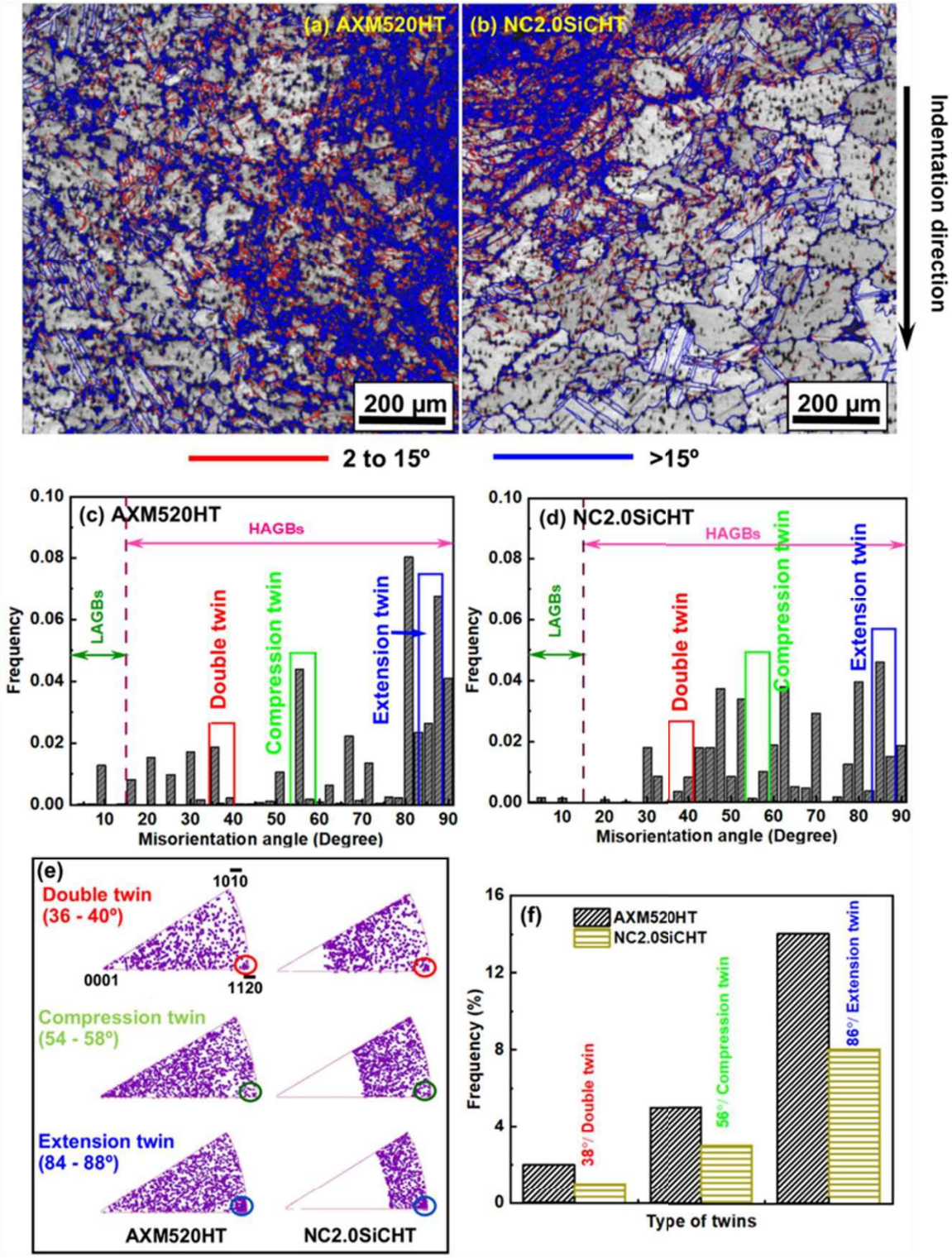

Figure 8.7 EBSD GB maps captured from the highly deformed corner regions of (a) AXM520HT and (b) NC2.0SiCHT; (c) and (d) misorientation map corresponding to 'a' and 'b', respectively; (e) IPF maps for the twins observed in AXM520HT and NC2.0SiCHT; and (f) comparison of twin fractions in creep-tested (T = 498 K, σ = 435 MPa) AXM520HT and NC2.0SiCHT.

to c-axis rotation along <1$\bar{2}$10> direction in both cases. Further, the SAED pattern indicates a massive sub-grain formation or dislocation accumulation around the TB during formation of this double twin. The occurrence of the dislocation pile-ups around the TB is depicted by the strain contrast in Figure 8.8(c).

The analyses of the dislocations present in the creep-tested specimen of the NC2.0SiCHT were carried out using two-beam condition **g.b**=0. The **'g'** corresponds to the diffraction vector, and b is known to be the burgers vector. In this condition, while a crystal is diffracted along **g**=0002, the dislocations with **b**=<0001> are visible in both BF and DF images by satisfying the criteria **g.b≠0**. These dislocations are known as <c> type dislocations. In the same region, the <a> type dislocations with **b**=<11$\bar{2}$0> were not visible with **g**=0002 when **g.b**=0 is satisfied. However, if the same area is seen along the **g**=10$\bar{1}$0 direction, the <a> type dislocations will be visible in both BF and DF images. On the other hand, the dislocations with **b**=<11$\bar{2}$3> will appear with both the **g** vectors (i.e., **g**= 0002 and **g**= 10$\bar{1}$0) as **g.b**≠0. These types of dislocations are known as <c+a> dislocations. The BF and DF images taken from the NC2.0SiCHT in Figure 8.9(a and c) displayed the <a> and <c+a> dislocation when exited along **g**=10$\bar{1}$0. The same region was also observed by exciting **g**=0002, as shown in Figure 8.9(b and d). The <c> and <c+a> dislocations were observed in both the BF and DF images. Interestingly, the <c+a> dislocations were observed in all the images at the same position under all the conditions, confirming their existence. A careful observation of Figure 8.9(a and b) reveals that the density of the <c> type dislocations was much higher than that of the <a> type dislocations. It is reported that the <a> type dislocations are associated with the low critical resolved shear stress (CRSS), which allowed them to glide easily during deformation [160]. In the process, the dislocation annihilation took place that resulted in the reduced dislocation density of <a> type. On the contrary, the higher value of CRSS of the <c> type dislocation made them sessile. A schematic of the <c+a> dislocation's dissociation into glissile <a> and sessile <c> dislocations is portrayed in Figure 8.9(e). After dissociation of the <c+a> dislocations at the intersection of the non-basal and basal planes, the <a> component easily glide in the closed packed basal plane, whereas the <c> type dislocation remained in the pyramidal or prismatic plane (i.e., non-basal plane), contributing to the strain hardening. The BF and DF images in Figure 8.9(f and g) exhibited that the dislocation bowed due to the presence of SiC_{np}. The dislocations in NCs had to overcome the additional stress field associated with the SiC_{np} phase. Thus, the creep resistance of the NCs was higher compared to the AXM520HT.

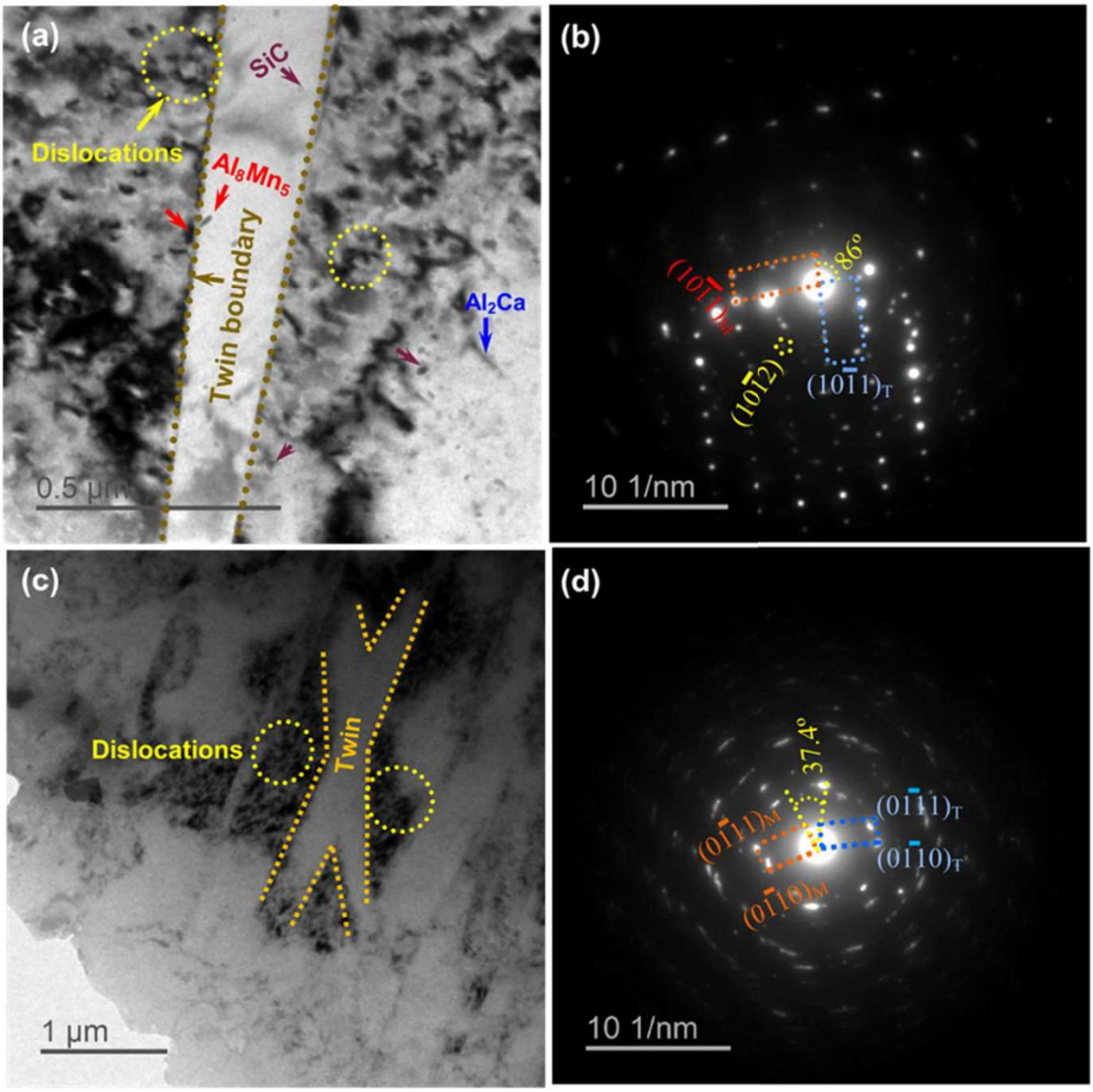

Figure 8.8 (a) BF image exhibiting an extension twin of type $\{10\bar{1}2\}<10\bar{1}1>$ taken from creep-tested NC2.0SiCHT; (b) SAED pattern corresponds to 'a'; (c) BF image exhibiting a double twin of type $\{10\bar{1}1\}$-$\{10\bar{1}2\}$ taken from creep-tested AXM520HT; (d) SAED pattern corresponds to 'c'.

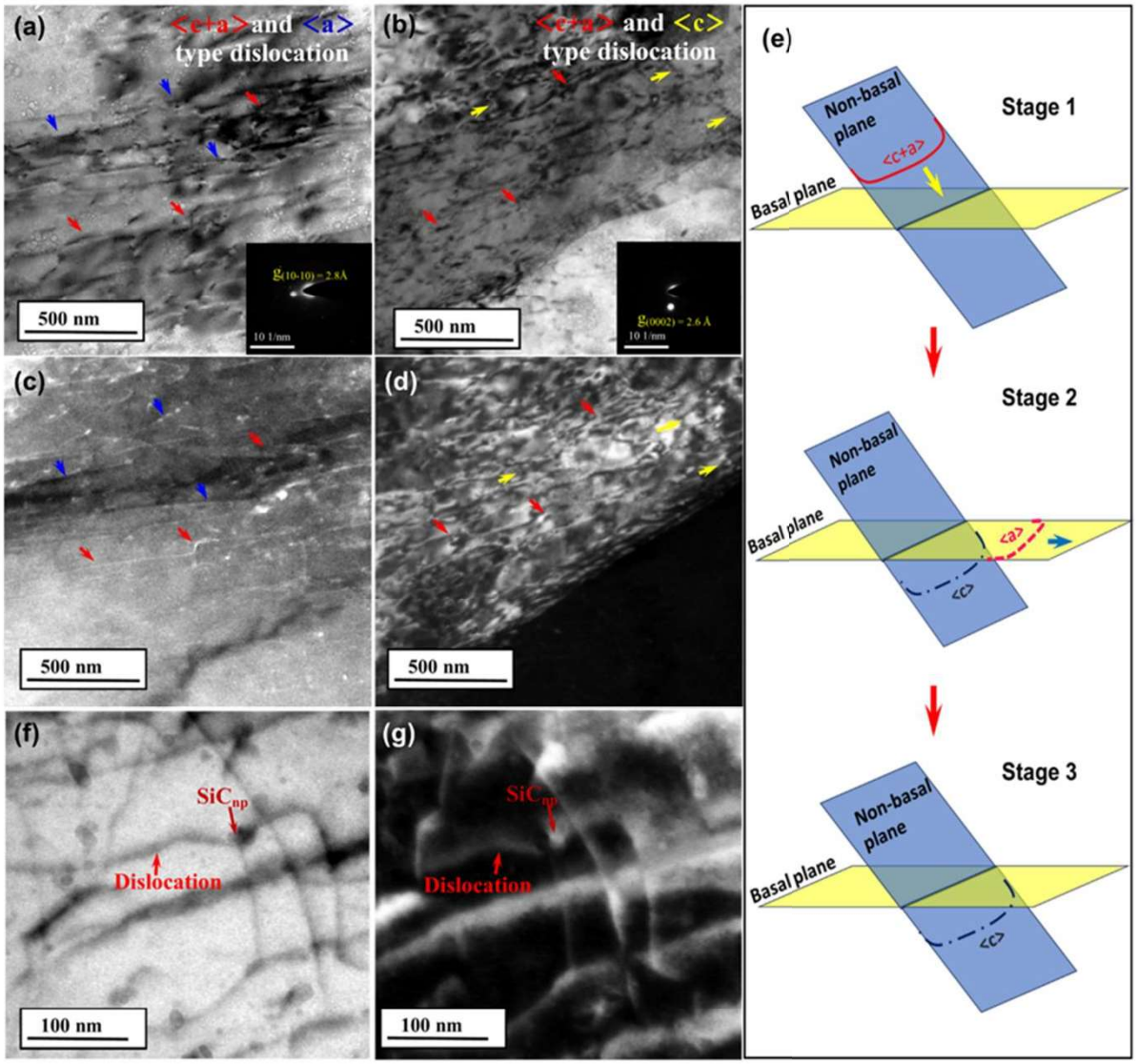

Figure 8.9 (a) and (c) BF and DF images of the <c+a> and <a> type dislocations while **g** = $10\bar{1}0$; (b) and (d) BF and DF images of the <c+a> and <a> type dislocations while **g** = 0002 in the same location taken from creep-tested NC2.0SiCHT; (e) schematic exhibiting <c+a> dislocation's dissociation into <a> and <c> type dislocations; (f) and (g) BF and DF image of the dislocation interaction with SiC_{np} in NC2.0SiCHT creep teste at 435 MPa and 473 K.

8.5 Summary of chapter 8

In the present chapter, the microstructural alteration and creep characteristic of the squeeze-cast age-hardened Mg-5.0Al-2.0Ca-0.3Mn (AXM520HT) alloy, as well as AXM520HT+1.0SiC (NC1.0SiCHT) and AXM520HT+2.0SiC (NC2.0SiCHT) (wt.%) nanocomposites (NCs) has been presented. The major findings from the current chapter are summarized below.

i. The age-hardened AXM520HT, NC1.0SiCHT, and NC2.0SiCHT contain the primary α-Mg grains, the discontinuous $(Mg, Al)_2Ca$ (C36) phase at the grain boundaries, and randomly present spherical-shaped Al_8Mn_5 phase. All the NCs additionally contain SiC phase.

ii. The NCs revealed superior creep resistance compared to AXM520HT, and it was the best in the NC2.0SiCHT. The improvement was 76% in NC2.0SiCHT compared to AXM520HT.

iii. The creep deformation was dominated by Dislocation climb facilitated by pipe diffusion at the chosen test temperature and stress ranges. The newly constructed maps could be used as a reference to predict the creep deformation mechanism for a particular stress, temperature, and grain size range for the Mg-Al-Ca-based alloys and NCs.

iv. The C36 phase was utterly broken in the AXM520HT, whereas the same remains intact in the NC2.0SiCHT. The percentage of twins in the creep-tested specimen of NC2.0SiCHT was lower than in the AXM520HT alloy. The density of the <c> type dislocations was much higher than that of the <a> type dislocations in the NCs.

v. The significant improvement in creep resistance of all the NCs over the AXM520HT alloy was attributed to the age-hardening as well as dispersion strengthening from the nanoparticles.